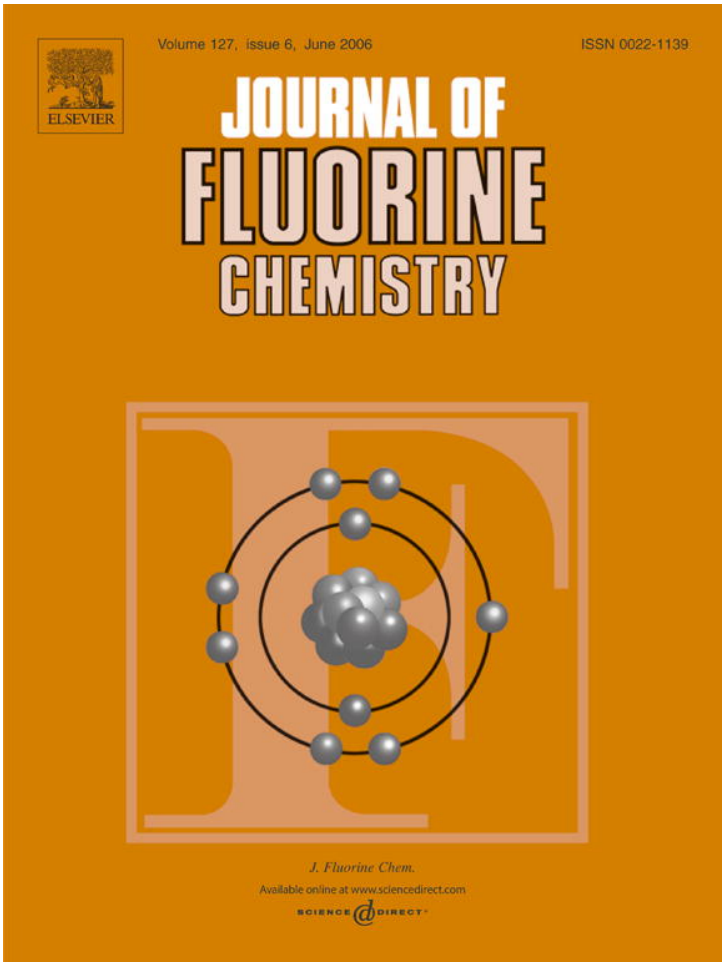

Available online at www.sciencedirect.com
SCIENCE DIRECT
Journal of Fluorine Chemistry 127 (2006) 787–795
JOURNAL OF FLUORINE CHEMISTRY
www.elsevier.com/locate/fluor

Estimation and analysis of the rheological properties of a perfluoropolyether through molecular dynamics simulation

Bangwu Jiang, David J. Keffer *, Brian J. Edwards

Department of Chemical Engineering, University of Tennessee, Knoxville, TN 37996-2200, United States

Received 6 January 2006; received in revised form 16 February 2006; accepted 16 February 2006
Available online 3 April 2006

Abstract

Equilibrium and non-equilibrium molecular dynamics simulations of a perfluoropolyether $C_8F_{18}O_4$ are reported using an atomistic interaction potential. The bulk rheological properties of the perfluoropolyether are investigated through molecular dynamics simulations as a function of both temperature and shear rate. The effect of molecular structure on viscosity is explored in detail. The rotational relaxation time is reported as a function of temperature. Structural properties, including the mean-square end-to-end chain length, the mean-square radius of gyration of chains, and the distribution functions of bond lengths, bond angles, and bond torsional angles are collected and analyzed as functions of shear rate. After an initial plateau, both mean-square end-to-end chain length and mean-square radius of gyration decrease monotonically with increasing shear rate. The behaviors of the rheological and structural properties are explained through an analysis of the individual contributions due to bond stretching, bond bending, and bond torsion, as well as both intramolecular and intermolecular non-bonded interactions. A further analysis is possible through a meticulous breakdown of each contribution into a specific type of mode; e.g., the total bond stretching is comprised of CC, CO, and CF bond stretching terms. In this way, one can relate the shear viscosity to the specific chemical structure of $C_8F_{18}O_4$.

Keywords: Perfluoropolyether; Rheology; Molecular dynamics; Simulation

1. Introduction

Perfluoropolyethers (PFPEs) form a class of lubricants, which are broadly applied in oxygen service, in aircraft instrument bearings, in reactive chemical environments, in vacuum pumps, in sealed-for-life electric motors, in computer hard drives, and as high-temperature greases. They possess numerous advantageous properties including chemical inertness, thermal, oxidative and hydrolytic stability, non-flammability, radiation resistance, shear stability, low vapor pressure, broad insolubility, and excellent lubricity under normal, severe, and starved operation conditions such as under heavy loads, at high speeds, and at elevated temperatures [1].

The commercially available PFPEs include Krytox, Fomblin, and Demnum. The PFPE fluids and greases have been well studied from an experimental point of view. There are many publications on experimental determination of the rheological properties of PFPE fluids (see, for example, Refs. [1–3]). There is a general, macroscopic understanding of the structure–property relationship of the constituent units in PFPE molecules and the rheological behavior. For example, as the amount of branching and the size of the substituent increase, the viscosity-temperature dependence will be adversely affected [3,4]. However, the properties of lubricants measured experimentally combine the effect of various aspects of molecules, such as orientation and intermolecular and intramolecular interactions. The effect of molecular architecture on the rheological properties of lubricants will dramatically influence their performance. A more detailed understanding of the atomistic structure–bulk property relationship will improve our ability to design new lubricants.

Previously, molecular dynamics (MD) simulations have been used successfully to obtain detailed information about the relationship between the viscosity and one specific aspect of molecular structure, chain length, in normal alkanes for both shear and elongational flows [5–7]. Specifically in Ref. [6], Baig et al. examined the individual contributions of five modes (bond stretching, bond bending, bond torsion, intramolecular Lennard–Jones interactions, and intermolecular Lennard–Jones interactions) for decane, hexadecane, and tetracosane under planar elongational flow. Baig et al. used a united-atom

* Corresponding author. Tel.: +1 865 974 5322; fax: +1 865 974 7076.
E-mail address: dkeffer@utk.edu (D.J. Keffer).

0022-1139/$ – see front matter © 2006 Published by Elsevier B.V.
doi:10.1016/j.jfluchem.2006.02.011

potential so that there was only one type of particle in their system, and no further analysis was possible or necessary. The analysis in this current work goes one step further because there are three types of atoms, and thus a further break can be made between the bond stretching contribution into CC, CO, and CF terms, the bond bending component into COC, CCO, OCF, CCF, and FCF terms, and the bond torsional component into COCC, COCF, OCCO, FCCO, and FCCF terms. By identifying each specific contribution to the viscosity, one can hope to use a ''group contribution'' approach to predicting the viscosity for PFPEs with other chemical formulae.

In comparison to hydrocarbons, the molecular simulation of fluorinated molecules is less developed partly due to the availability of an interaction potential. Several groups applied molecular simulation to PFPE fluids. Li et al. parameterized a united-atom potential based on the short-chain perfluoroalkanes and perfluoroethers [8,9]. McCabe et al. calculated viscosities and other transport properties of perfluoroalkanes through molecular simulation for both explicit-atom and united-atom force fields [10]. They found that an explicit-atom model could predict the Newtonian viscosity of short perfluoroalkanes in most cases within experimental error; however, the united-atom model underpredicted the viscosity. For this reason, we have employed an explicit-atom interaction potential in this work.

Koike used molecular dynamics to study the tribological behaviors of branched and linear PFPEs confined by two rigid surfaces of a face-centered cubic Ni lattice [11]. He found that the viscosity of the branched Krytox type is slightly lower than that of the linear Demnum when confined. Kamei et al. studied the dynamic properties of three types of perfluoropolyethers confined by two rigid surfaces of a Fe lattice [12]. Frictional coefficients were reported at different temperatures. To date, no systematic set of molecular simulations for the bulk rheological properties of PFPEs have been published.

In this work, we use an explicit-atom force field, the Universal Force Field (UFF) [13], to study one linear perfluoropolyether (PFPE-Z) compound $C_8F_{18}O_4$ (CF_3–O–CF_2–CF_2–O–CF_2–CF_2–O–CF_2–CF_2–O–CF_3) at equilibrium and under an imposed shear flow field at different temperatures. The equilibrium molecular structure is shown in Fig. 1.

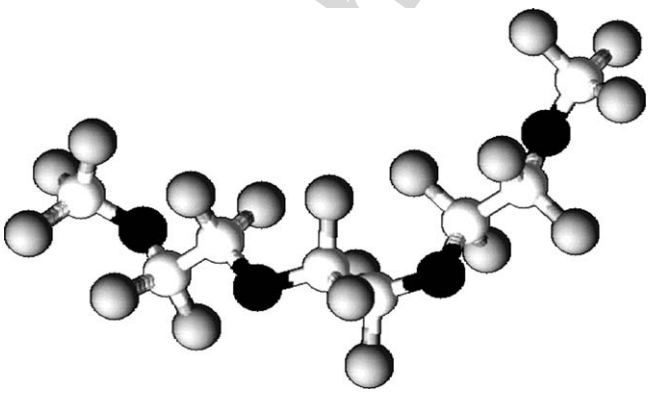

Fig. 1. The molecular structure of a single molecule $C_8F_{18}O_4$. Oxygen atoms are black, carbon atoms are white, and fluorine atoms are gray.

Rheological properties such as the shear viscosity and the first normal stress coefficient, are reported. Changes in the structural and energetic properties of the molecule as functions of temperature and shear rate are also reported. The potential information and simulation techniques are described in Section 2. The results and discussion are given in Section 3, and conclusions are presented in Section 4.

2. Molecular model and simulation methods

2.1. Interaction potential

The model we used is the well-known Universal Force Field, which was developed by Rappe et al. [13]. The form of the UFF for the intramolecular force is expressed as

$$E_{\text{pot}} = E_{\text{R}} + E_{\theta} + E_{\phi} + E_{\text{vdw}} \tag{1}$$

The potential energy consists of contributions from bond stretching, E_{R}, bond angle bending, E_{θ}, dihedral angle torsion, E_{ϕ}, and both intramolecular and intermolecular non-bonded van der Waals interactions, E_{vdw}. We do not explicitly account for partial charges in the system, since the UFF potential has incorporated that effect into the parameters. In UFF, the bond stretching energy assumes a Hookean spring,

$$E_{\text{R}} = \frac{1}{2}K_{ij}(r - r_{ij})^2 \tag{2}$$

where K_{ij} is the force constant for bond stretching and r_{ij} is the equilibrium bond length between atoms i and j. The bond angle bending energy is a cosine expansion,

$$E_{\theta} = K_{ijk}(C_0 + C_1\cos\theta + C_2\cos^2\theta) \tag{3}$$

where K_{ijk} is the force constant for bond bending, and the three expansion coefficients are defined as functions of the equilibrium bond angle, θ_0: $C_2 = 1/(4\sin^2\theta_0)$, $C_1 = -4C_2\cos\theta_0$, and $C_0 = C_2(2\cos^2\theta_0 + 1)$. The torsion energy is expressed as

$$E_{\phi} = \frac{1}{2}V_{\phi}(1 - \cos n\phi_0\cos n\phi) \tag{4}$$

where V_{ϕ} is the rotational barrier and n is the periodicity of the torsion potential. Finally, the non-bonded interaction is of the form

$$E_{\phi} = \varepsilon_{ij}\left[\left(\frac{\sigma_{ij}}{r}\right)^{12} - 2\left(\frac{\sigma_{ij}}{r}\right)^{6}\right] \tag{5}$$

where ε_{ij} is an energetic parameter and σ_{ij} is the collision diameter. The non-bonded interaction is applied to two atoms in the same molecule separated by at least two atoms; e.g., it excludes atoms interacting through the stretching or bending potentials. The same functional form and parameters are used to describe the intermolecular non-bonded interactions. The potential parameters are listed in Table 1. The Lorentz–Berthelot combination rules, $\varepsilon_{ij} = (\varepsilon_i\varepsilon_j)^{1/2}$ and $\sigma_{ij} = (\sigma_i + \sigma_j)/2$, are used for the non-bonded interaction between atoms of different types.

Table 1
List of interaction potential parameters

Atom type	ε/k_B (K)	σ (Å)
C	52.84	3.851
F	25.16	3.364
O	30.19	3.500
Bond	K_{ij}/N_A (aJ Å^{-2})	r_{ij} (Å)
C–C	4.861	1.514
C–O	7.044	1.423
C–F	5.100	1.442
Angle	K_{ijk}/N_A (aJ rad^{-2})	θ_0 (°)
C–C–O	2.086	109.47
C–C–F	1.545	109.47
C–O–C	2.045	104.51
F–C–O	1.917	109.47
F–C–F	1.417	109.47
Torsion	V_ϕ/N_A (aJ)	ϕ_0 (°)
CO	1.347E−3	3.180
CC	1.472E−2	3.180

2.2. Simulation methods

For the NVT equilibrium molecular dynamics simulations (EMD) and the non-equilibrium molecular dynamics simulations (NEMD), the multiple time-step method developed by Tuckerman et al. [14] was combined with a Nosé–Hoover thermostat [15–17] to integrate the equations of motion. NVT EMD was used to estimate the relaxation time of the system and to generate the initial configuration for NVT NEMD. For the NEMD case of planar Couette flow, the trajectories of the particles can be generated with the SLLOD algorithm [18] (which is equivalent in shear flow to the p-SLLOD algorithm [19]). The equations of motion are

$$\begin{aligned}\dot{q}_{ia} &= \frac{p_{ia}}{m_{ia}} + q_{ia}\cdot\nabla u \\ \dot{p}_{ia} &= F_{ia} - p_{ia}\cdot\nabla u - \frac{p_\zeta}{Q}p_{ia} \\ \dot{p}_\zeta &= \sum_i\sum_a \frac{p_{ia}^2}{m_{ia}} - fk_BT\end{aligned} \tag{6}$$

where p_{ia} and q_{ia} are the momentum and position vectors of atom a of molecule i, respectively, and F_{ia} is the force vector on the atom a of molecule i with mass m_{ia}. f is the number of degrees of freedom in the system, T the absolute temperature, and k_B is the Boltzmann constant. p_ζ and Q are the momentum-like variable and inertial mass parameter of the Nosé–Hoover thermostat.

The equations of motion were integrated through the reversible reference system propagator algorithm (r-RESPA) [14] with two time scales. The large time step of 2.0 fs was used for the intermolecular interactions and thermostat, and the small time step of 0.20 fs was used for the intramolecular interactions. The Lees–Edwards [20] periodic boundary condition was applied to the system with 216 $C_8F_{18}O_4$ molecules. A cut-off distance of 12.5 Å ($3.25\sigma_{CC}$) was used for all the Lennard–Jones van der Waals interactions. The pour

Table 2
The state points and the relaxation times for $C_8F_{18}O_4$

T (K)	253	273	293	313	333	353	373
Density (g/ml)	1.69	1.65	1.62	1.59	1.56	1.53	1.50
τ (ps)	3060	1696	893	632	429	329	213

points of most PFPEs with molecular weights of 1500 g/mol are about −58 °C, and generally the pour point decreases with the increasing molecular weight [21]. Therefore, it is fair to say that, at the lowest temperature investigated (253 K), we are well above the pour point of $C_8F_{18}O_4$. The compound under investigation was synthesized through aerosol direct fluorination [22]. It has a boiling point 105.6 °C at 757 mmHg, and a density of 1.62 g/ml at 293 K, which were experimentally measured by Crawford and Adcock [23]. Four temperatures (253, 293, 333, and 373 K) were studied in both EMD and NEMD NVT simulation. The state points listed in Table 2 at the other temperatures were estimated through use of the coefficient of thermal expansion, 0.001 °C^{-1}, reported by Bell et al. [1].

In the NEMD calculations, the strain-rate dependent viscosity, η, is determined from the constitutive relation

$$\eta = -\frac{\Pi_{xy}}{\dot{\gamma}} \tag{7}$$

Here, the x direction is chosen as the flow direction and y direction as the flow gradient direction, implying that the shear rate is $\dot{\gamma} = \partial u_x/\partial y$, where u_x is the streaming velocity in x direction. Π_{xy} is the xy component of the pressure tensor, Π, which is calculated as [18]

$$\Pi = \left\langle \frac{1}{V}\sum_i\sum_a \left(\frac{p_{ia}p_{ia}}{m_{ia}} + q_{ia}F_{ia} \right) \right\rangle \tag{8}$$

The angular brackets denote the time average of the system trajectory.

3. Results and discussion

3.1. The estimation of the relaxation time from NVT EMD simulation

After the NVT EMD simulation reaches equilibrium, the normalized end-to-end distance vector, $\tilde{R}_{ete}$, of each molecule was sampled along the system trajectory. The time autocorrelation function, $\psi(t)$, of the end-to-end distance vector is defined as [24]

$$\psi(t) = \frac{1}{mn}\sum_k^m\sum_i^n \tilde{R}_{ete(i)}(t_k)\tilde{R}_{ete(i)}(t_k + t) \tag{9}$$

Here, m is the total number of available time origins, n the number of molecules in the system, and t is the delay time. The exponential functional form $\psi(t) = A\exp(-t/\tau)$ is used to fit the time autocorrelation function simulation results to obtain the rotational relaxation time, τ. The long-time tail was observed in our system, as mentioned in Ref. [24]. In Fig. 2, we plot $\psi(t)$ from both simulation and fitting as a function of delay time at

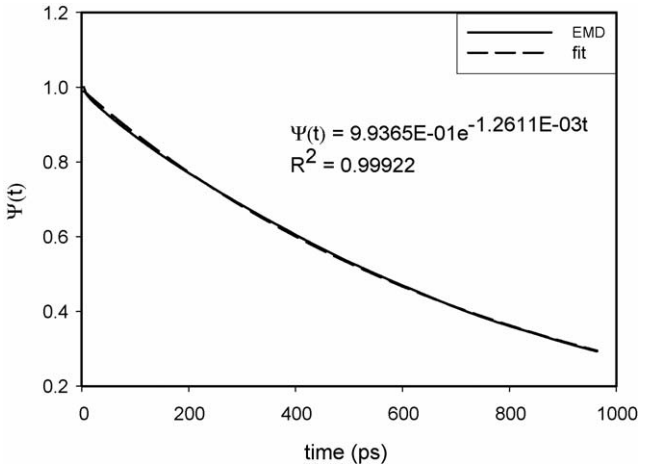

Fig. 2. The time autocorrelation function $\psi(t)$ of the end-to-end distance vector as a function of time at 293 K.

the temperature of 293 K. Clearly, $\psi(t)$ decreases exponentially to about 0.3. Following convention, we do not include the long-time tail in the exponential fit. From this plot, we obtain the relaxation time of this compound at 293 K, which is 792 ps. Similarly, we can calculate the relaxation times for the different temperatures, which are listed in Table 2.

The site-model theory [25] states that the temperature dependence of the relaxation time, which is equivalent to the average time between jumps over the barrier, can be described by the Arrhénius equation, $\tau = A_0 \exp[\Delta E/(RT)]$. From the Maxwell Model of viscoelasticity [26], we know $\eta_0 = nRT\tau$, where n is the number density of chains. If we ignore the temperature change of nRT, the zero-shear viscosity is approximately proportional to relaxation time. In Fig. 3, we plot ln τ and ln (η_0) versus 1/T. From these plots, we observe that the rotational relaxation time and zero-shear viscosity of compound $C_8F_{18}O_4$ generally obey the Arrhénius equation. From the fitting, we can also obtain the activation energy for the rotation of this molecule as 228 J/mol and the activation energy for zero-shear viscosity as 217 J/mol, which is very close to that of relaxation time; therefore, we can say that the zero-shear viscosity is nearly proportional to relaxation time.

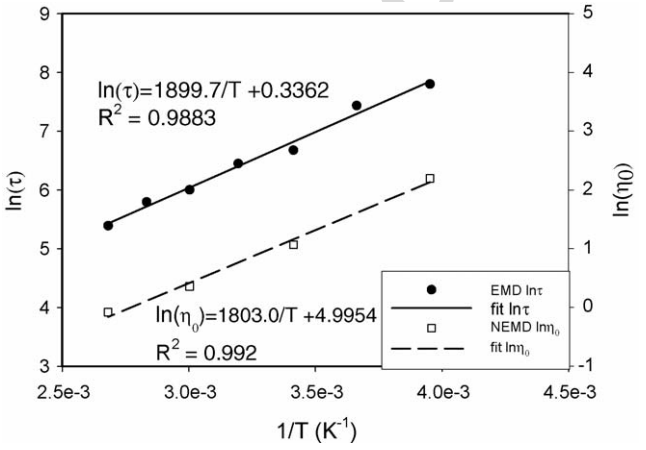

Fig. 3. The relaxation time and zero-shear viscosity as a function of temperature from MD simulation and fitting to the Arrhénius equation.

3.2. The rheological properties and energetic responses under shear

In Table 3, we list the NEMD simulation results of shear viscosity, η, as a function of the shear rate for $C_8F_{18}O_4$ at four different temperatures and the simulation run lengths. All the NEMD simulations started from initial configurations created and well equilibrated through the EMD simulations. The NEMD run lengths varied due to the differences in relaxation times (as a result of the different temperatures) and due to the differences in shear rate.

In Fig. 4, we plot the shear viscosity as a function of the shear rate, $\dot{\gamma}$. The vertical lines represent the critical shear rates calculated as the inverse of relaxation times collected in Table 2. The critical shear rate is usually considered as the boundary between the Newtonian and non-Newtonian regions. Fig. 4 shows that shear-thinning behavior does begin near the critical shear rate at each temperature. To our knowledge, there is no viscosity data reported for this specific compound in literature, although Koike [11] presented some viscosity data for other PFPE compounds from MD simulation under confined conditions, and these viscosities also were reported as several orders of magnitude larger than the shear viscosity for a bulk system. Bell et al. [1] reported some general viscosity data for Krytox PFPE oils at 331 K for different molecular weights. Using this data, we can estimate the viscosity for this molecule through the simple power–law relation between viscosity and molecular weight. We obtain the viscosity 1.5 cp when the molecular weight is 502 g/mol; therefore, the value (2.0 cp) that we have obtained at 333 K seems very reasonable. Fig. 4 also shows that the shear viscosity decreases and that the critical shear rate increases with increasing temperature, as expected. The difference in the shear viscosity between the temperatures is fairly significant at low shear rates, but decreases with increasing shear rate.

The shear rate dependence of the first normal stress difference coefficient, ψ_1, is shown in Fig. 5. ψ_1 decreases with increasing temperature and shear rate. The trend is similar to the shear viscosity, except that at low shear rates the viscosity for all the temperatures examined displays the Newtonian plateau, but the first normal stress coefficient does not. However, we cannot make any definitive conclusion because of the large statistical uncertainty of ψ_1 at low shear rates.

In Fig. 6, we present the contribution of the different modes in the interaction potential to the viscosity as functions of shear rate. The contributions from bond stretching and bond bending are large and positive. The contribution from the intramolecular non-bonded interaction is large and negative, compared with the total viscosity. The total contribution from these three interactions largely offset each other, since the total viscosity is small by comparison. The intermolecular non-bonded interactions contribution to the total viscosity is small and negative. The torsion contribution is small and positive.

In the presence of a flow field, the intramolecular and intermolecular configurations change from the equilibrium state in order to minimize the free energy in the presence of the external field. Consequently, the distribution functions of the

Table 3
Shear viscosity as function of shear rate for compound $C_8F_{18}O_4$ at four different temperatures

253 K			293 K		
Shear rate (s^{-1})	Viscosity (cp)	Run length (ns)	Shear rate (s^{-1})	Viscosity (cp)	Run length (ns)
6.6×10^{10}	0.771 (3)	19.0	1.0×10^{11}	0.500(3)	8.2
3.3×10^{10}	1.09(2)	19.0	6.6×10^{10}	0.60(2)	8.2
1.0×10^{10}	2.04(2)	19.0	3.3×10^{10}	0.792(5)	10.0
6.6×10^{9}	2.38(9)	19.0	1.0×10^{10}	1.36(5)	12.0
3.3×10^{9}	3.4(1)	19.0	6.6×10^{9}	1.59(3)	15.0
1.0×10^{9}	5.7(5)	26.0	3.3×10^{9}	2.08(2)	18.0
6.6×10^{8}	6.2(5)	26.0	1.0×10^{9}	2.48(7)	20.0
3.3×10^{8}	7.2(3)	56.0	6.6×10^{8}	2.9(1)	20.0
1.0×10^{8}	9.6(1.0)	68.0	3.3×10^{8}	2.7(2)	23.0
6.6×10^{7}	7.6(2.0)	68.0	1.0×10^{8}	3.1(7)	25.0
3.3×10^{7}	9.8(3.2)	68.0			
333 K			373 K		
Shear rate (s^{-1})	Viscosity (cp)	Run length (ns)	Shear rate (s^{-1})	Viscosity (cp)	Run length (ns)
1.0×10^{11}	0.412(7)	6.2	1.0×10^{11}	0.332(8)	2.5
6.6×10^{10}	0.478(8)	6.2	6.6×10^{10}	0.395(10)	2.5
3.3×10^{10}	0.63(2)	7.2	3.3×10^{10}	0.481(7)	3.5
1.0×10^{10}	1.04(3)	8.0	1.0×10^{10}	0.71(3)	3.5
6.6×10^{9}	1.22(5)	12.0	6.6×10^{9}	0.81(3)	3.5
3.3×10^{9}	1.40(6)	12.0	3.3×10^{9}	0.91(10)	5.5
1.0×10^{9}	1.43(6)	48.0	1.0×10^{9}	0.87(4)	44.0
6.6×10^{8}	1.34(9)	51.0	6.6×10^{8}	0.91(6)	48.0

Numbers in parentheses represent the statistical uncertainties.

bond lengths, bending angles, and torsion angles change from their equilibrium values as well. These changes are reflected in the viscosity. As expected, the total viscosity is constant in the region of the Newtonian plateau. At very low shear rate values, the individual contributions drop sharply, and then remain constant for a while; after this, they tend toward zero (either shear-thinning for positive contributions or shear-thickening for negative contributions) beyond the critical shear rate.

Since bond stretching and bond bending are two important factors in the total viscosity, we present the contribution to the viscosity due to each type of stretching and bending interaction in Figs. 7 and 8, respectively. Again, we see that the individual types of bond stretching and bond bending modes drop sharply at very low shear rates, and then remain constant within the Newtonian plateau. Beyond the critical shear rate, the individual contributions approach zero.

Fig. 7 also shows that the contributions from CO bond stretching are large and positive, CF are large and negative, and CC are small and positive. This behavior cannot be explained by the magnitude of the bond stretching force constants, K_{ij}, given in Table 1, in which the CO parameter is largest. Instead we can consider the following argument. At equilibrium, the

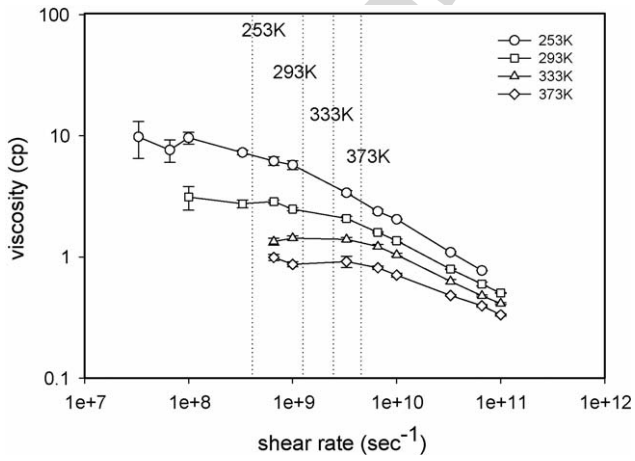

Fig. 4. The shear viscosity as a function of shear rate at different temperatures. The vertical lines stand for the critical shear rate for the corresponding temperatures.

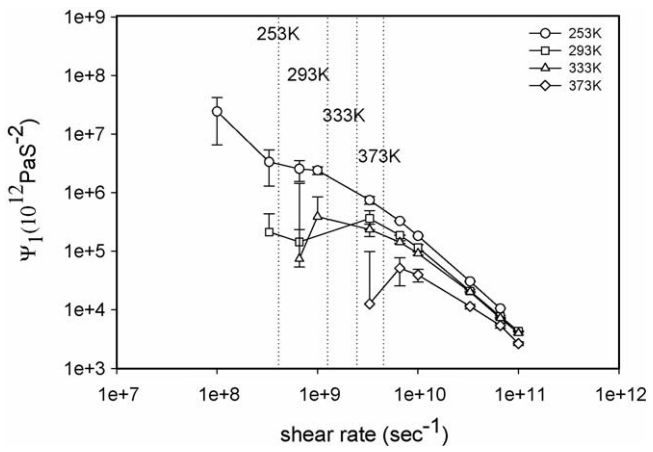

Fig. 5. The first normal stress coefficient as a function of shear rate at different temperatures. The vertical lines stand for the critical shear rate for the corresponding temperatures.

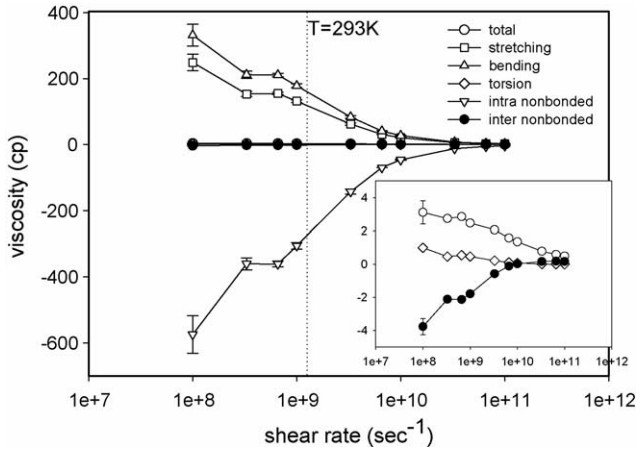

Fig. 6. The contribution of the different interactions to the viscosity as functions of shear rate at 293 K. The vertical line stands for the critical shear rate.

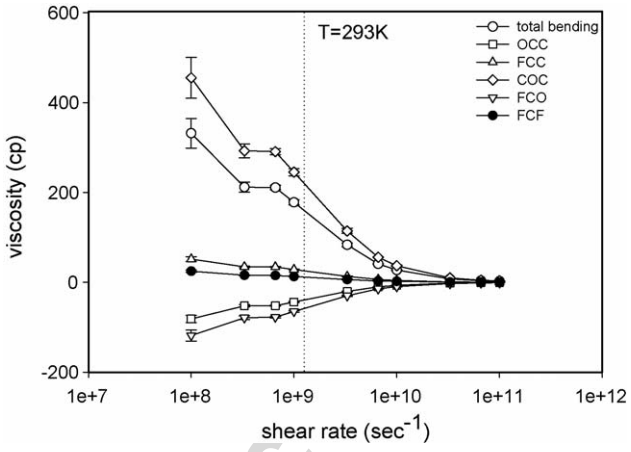

Fig. 8. The contribution of bending interactions to the viscosity as functions of shear rate at 293 K. The vertical line stands for the critical shear rate.

CO bond contribution to the *xy* component of the pressure tensor is larger in magnitude than the other bonds because they are not surrounded by fluorine atoms, which sterically impinge upon other fluorine atoms. The atoms in the CC and CF bonds are entirely surrounded by bonded and non-bonded fluorine atoms. This additional freedom of the oxygen atom allows the CO mode to vibrate in a less constrained environment, resulting in a larger contribution to the pressure tensor. That the CC bond yields a positive contribution to the viscosity indicates that the CC bond stretching force is positive, meaning the interaction is repulsive on average and the average bond length is compressed below the equilibrium length. Similarly, the CF bond contributes negatively, indicating that the average CF bond length must be greater than the equilibrium bond length, thus resulting in an attractive force. Further study and comparison to other molecules is needed to explain completely this behavior.

In Fig. 8, we see that the COC segment dominates the contribution to the viscosity from bond bending. The OCC and FCO make large and negative contributions to the viscosity. The contributions from FCC and FCF are relatively small. This information explains partly why the viscosity of PFPE is almost five times larger than that of the corresponding perfluoroalkanes [10]. The division of rheological properties according to the type of interactions can help us understand property–structure relationships from the atomistic scale. This knowledge may guide us to design new materials with better rheological properties, especially when more compounds with similar but distinct structures are explored.

McCabe et al. [10] compared the united-atom and explicit-atom models for perfluoroalkanes. They found that the explicit-atom model predicts the zero-shear viscosity fairly well, whereas the united-atom model underpredicts it. The united-atom model is obviously missing some contributions to the viscosity including bond stretching from CF, bond bending from FCC, FCO, and FCF, and bond torsion from COCF, FCCO, and FCCF. It is natural to wonder if the missing contributions can account for the underprediction of the united-atom model. This comparison is complicated by the fact that the united-atom parameters for the backbone CF_2–CF_2 interactions do not correspond to explicit-atom backbone C–C interactions. With these disclaimers, we can proceed to examine Figs. 7 and 8. The contribution to viscosity from CF and FCO is negative and that from FCC, and FCF is positive, but the total contribution of interactions related to fluorine atom is negative. Seemingly, the conclusion would be that the united-atom model should overpredict the viscosity (if the backbone interactions were the same). It would be possible to parameterize a united-atom potential to capture these missing contributions, but whether this new model would have any predictive capability is not currently clear.

In Fig. 9, we present the potential energy as a function of shear rate at 293 K. The potential energy does not change substantially with shear rate. Fig. 9 also shows that the intramolecular non-bonded interactions give a positive (repulsive) energy, and that the intermolecular non-bonded interactions give a negative (attractive) potential energy. Of course, the stretching, bending, and torsion energies are positive since they are defined relative to a zero minimum energy configuration. The reason that the intramolecular non-bonded interaction is positive is due to the large size of the fluorine atoms.

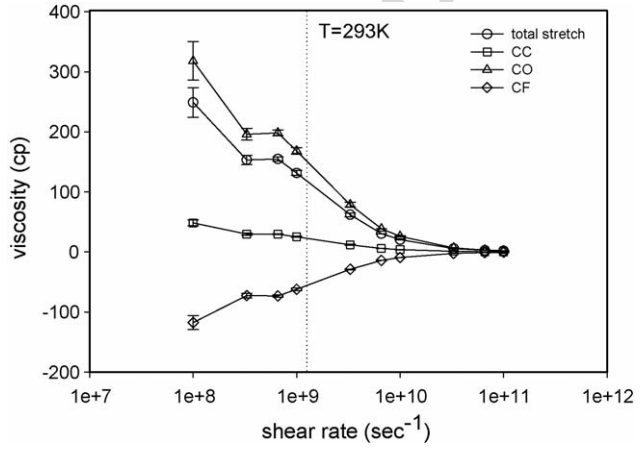

Fig. 7. The contribution of stretching interactions to the viscosity as functions of shear rate at 293 K. The vertical line indicates the critical shear rate.

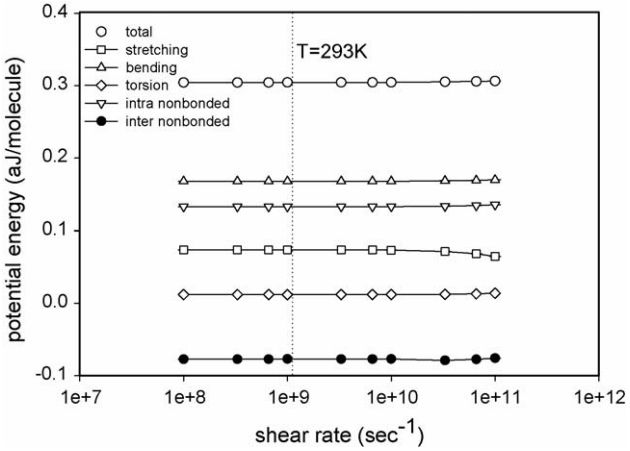

Fig. 9. The contribution of the different interaction to the potential energy as functions of shear rate at 293 K. The vertical line stands for the critical shear rate.

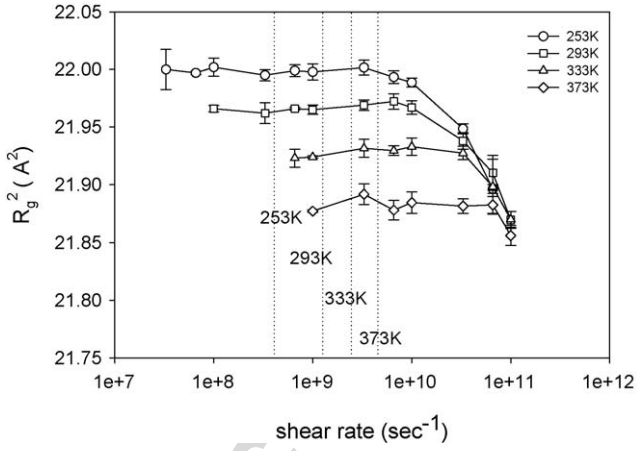

Fig. 11. The shear rate dependence of the mean-square chain radius of gyration, $\langle R_g^2 \rangle$, at the different temperatures. The vertical lines stand for the critical shear rates.

The relative insensitivity of the potential energy to the flow field is somewhat surprising. Baig et al. [6] reported significant change of potential energy for hydrocarbons in planar elongational flow. The different behavior of the potential energy can be attributed to the stiffness difference between hydrocarbons and PFPEs, which will be discussed in more detail shortly.

Two important structural quantities, the mean-square end-to-end distance of chains, $\langle R_{ete}^2 \rangle$, and the mean-square radius of gyration of chains, $\langle R_g^2 \rangle$, are presented as functions of shear rate at the different temperatures in Figs. 10 and 11, respectively. Since both $\langle R_{ete}^2 \rangle$ and $\langle R_g^2 \rangle$ are directly associated with the molecular conformations, they are expected to change similarly with the variation of the strength of the flow field. Indeed, Figs. 10 and 11 show this similarity. Both $\langle R_{ete}^2 \rangle$ and $\langle R_g^2 \rangle$ remain constant at low shear rates, and then decrease with increasing shear rate. The shear rate where $\langle R_{ete}^2 \rangle$ and $\langle R_g^2 \rangle$ start decreasing noticeably is higher than the corresponding critical shear rate; moreover, both $\langle R_{ete}^2 \rangle$ and $\langle R_g^2 \rangle$ change with shear rate less than 3 Å^2 at a specific temperature across the range of shear rates explored. This behavior for $C_8F_{18}O_4$ stands in sharp contrast to that of the hydrocarbons decane, hexadecane, and tetracosane reported by Cui et al. [27] under shear flow and Baig et al. [6] under planar elongational flow. Cui et al. [27] reported that $\langle R_g^2 \rangle$ increased at low shear rates and decreased at high shear rates, and that for decane $\langle R_g^2 \rangle$ did not change much at all. Baig et al. [6] reported an increasing trend for both $\langle R_{ete}^2 \rangle$ and $\langle R_g^2 \rangle$ with increasing flow strength; the changing magnitudes of $\langle R_{ete}^2 \rangle$ and $\langle R_g^2 \rangle$ are about 100 and 30 Å^2, respectively. From Figs. 10 and 11, we conclude that $C_8F_{18}O_4$ is very stiff and cannot be further stretched by shear flow in the same way that a hydrocarbon can.

This behavior can be further explained by examining the distribution of torsion angles, as has been done previously for hydrocarbons in elongational flow by Baig et al. [6]. In the case of hydrocarbons, the change in $\langle R_{ete}^2 \rangle$ and $\langle R_g^2 \rangle$ with strain-rate can be explained by examining the relative population of anti and gauche configurations of the CCCC torsion angle. From purely geometrical arguments, the anti state will have a longer end-to-end distance than the gauche state. For hydrocarbons, both the anti and gauche occupancies are on the same order of

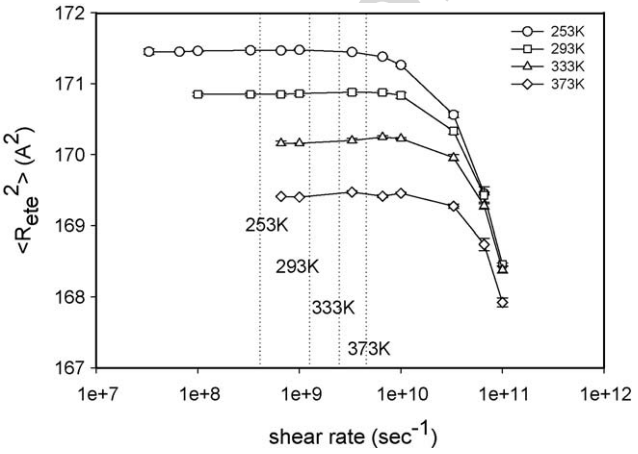

Fig. 10. The shear rate dependence of the mean-square chain end-to-end distance, $\langle R_{ete}^2 \rangle$, at the different temperatures. The vertical lines stand for the critical shear rates.

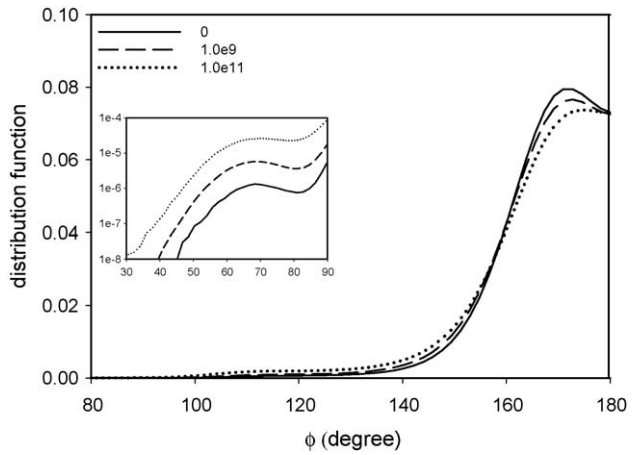

Fig. 12. The distribution function of the torsion angle ϕ of the C–O–C–C segment as a function of shear rate at the temperature 293 K.

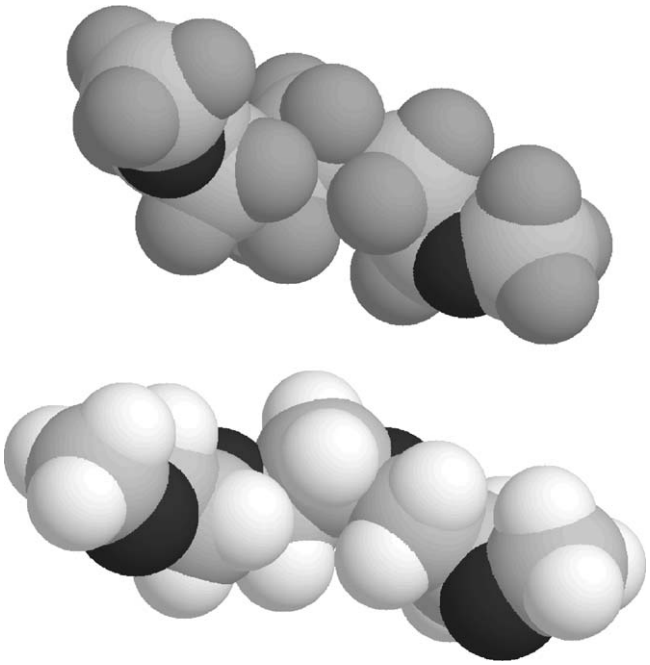

Fig. 13. Structure of $C_8F_{18}O_4$ (upper) and $C_8H_{18}O_4$ (lower) in a single-molecule environment.

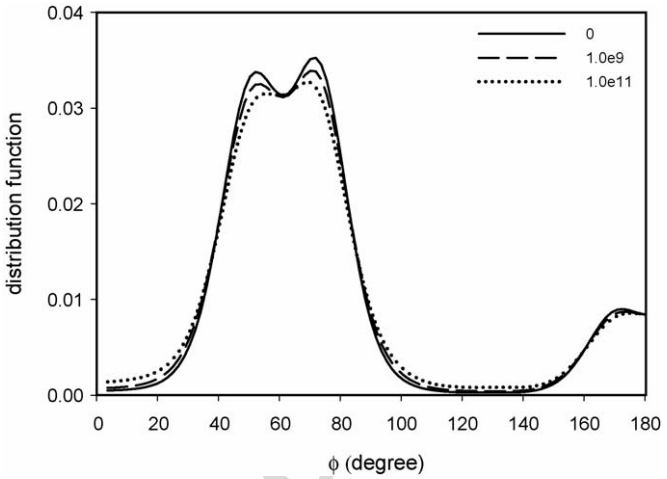

Fig. 14. The distribution function of the torsion angle ϕ of the COCF segment as a function of shear rate at the temperature 293 K.

magnitude at equilibrium. Thus it remains a possible that a flow field that results in a shift from gauche to anti will increase $\langle R^2_{ete}\rangle$ and $\langle R^2_g\rangle$, whereas a shift from anti to gauche will decrease $\langle R^2_{ete}\rangle$ and $\langle R^2_g\rangle$. However, in the PFPEs, we have a different situation. At equilibrium, the CCOC torsion angle (representing the configuration of the backbone) is virtually entirely in a distorted anti configuration. The fraction of angles in the distorted gauche configuration is over two orders of magnitude smaller, as shown in Fig. 12. Therefore, the possibility to shift from gauche to anti, thereby increasing $\langle R^2_{ete}\rangle$ and $\langle R^2_g\rangle$, does not exist. It is possible, if the flow field dictates it, to decrease $\langle R^2_{ete}\rangle$ and $\langle R^2_g\rangle$, but we see that for PFPE the driving force is not very strong. In Fig. 12, we see that the peak of the COCC torsion angle distribution is indeed broadening with increasing shear rate, resulting in the smaller values of $\langle R^2_{ete}\rangle$ and $\langle R^2_g\rangle$.

We now comment on the distortion of the anti and gauche peaks in Fig. 12. We observe in this figure that the peak of the distribution is slightly distorted from the anti angle, 180°, which is the natural torsion angle for COCC. The distortion is not observed in a similarly sized hydrogenated molecule, and can therefore be attributed to the presence of the fluorine. To illustrate this, we show in Fig. 13 a space-filling model of $C_8F_{18}O_4$ and the analogous compound, $C_8H_{18}O_4$. One can see that the fluorine atoms can overlap, whereas the hydrogen atoms cannot. We can also see the effect of this distortion on the FCOC torsion angle distribution in Fig. 14, in which both the gauche and anti conformations are distorted.

At shear rates where shear-thinning behavior is observed, we also observe alignment of molecular chains, as shown in Fig. 15, which is a snapshot of a slab of the simulation. Only a portion of the entire simulation box (a small number of the occupying molecules) is shown so as to allow for the alignment to be clearly distinguished.

Finally, we comment on the generality of the rheological and structural response of this compound. We expect that the trends of the total viscosity are relatively insensitive to potential. However, the distribution of contributions among types of modes, which are large and canceling, may change from one potential to the next, depending upon the balance between the various modes. Nevertheless, for the same potential, given the data presented in this paper, one can imagine a "group

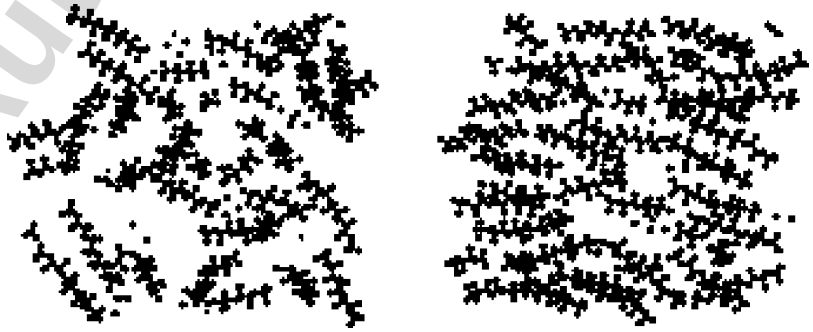

Fig. 15. Snapshot for $C_8F_{18}O_4$ from a simulation at 293 K: the left snapshot is from the EMD simulation, and the right one is from the NEMD simulation at a shear rate of $3.3 \times 10^{10}\ s^{-1}$.

contribution'' approach to estimating the viscosity of similar compounds. The idea is as follows. In this work, we have demonstrated the contribution to viscosity per each type of stretching mode, CC, CO, and CF. If we divide these values by the number of each type of mode present per molecule, then we have a per-mode contribution from each type of mode. Predicting the viscosity of another PFPE can be performed simply by determining the number of each type of mode in the new molecule and multiplying it by the per-mode value. The same procedure can be repeated for the bond angle, torsion angle, and non-bonded interactions, which, when summed together, will yield a total viscosity. We are currently performing EMD and NEMD simulations of other PFPEs to test this concept.

4. Conclusions

We have reported the bulk rheological properties of a perfluoropolyether, $C_8F_{18}O_4$, through EMD and NEMD simulations with an atomistic potential. The bulk rheological properties of the perfluoropolyether were investigated as functions of both temperature and shear rate. The viscosity displayed shear-thinning behavior at all temperatures. The effect of molecular structure on viscosity was explored in detail. The rotational relaxation time was reported as a function of temperature. Structural properties, including the mean-square end-to-end chain length, the mean-square radius of gyration of chains, and the distribution functions of bond lengths, bond angles, and bond torsional angles, were collected and analyzed as functions of shear rate. After an initial plateau, both mean-square end-to-end chain length and mean-square radius of gyration decreased monotonically with increasing shear rate. The behavior of the rheological and structural properties was explained through an analysis of the individual contributions due to bond stretching, bond bending, bond torsion, and intramolecular and intermolecular non-bonded interactions. Further analysis was possible through a meticulous breakdown of each contribution into each specific type of mode; e.g., the total bond stretching is comprised of CC, CO, and CF bond stretching terms. In this way, we related the shear viscosity to the specific chemical structure of $C_8F_{18}O_4$. We further suggested that this procedure can lead to a predictive group contribution approach to the viscosity of PFPEs, which we are currently investigating.

Acknowledgements

This work has been supported by Air Force Office of Scientific Research through contract # FA 9550-05-1-0342. This research used resources of the Center for Computational Sciences at Oak Ridge National Laboratory, which is supported by the Office of Science of the DOE under Contract DE-AC05-00OR22725.

Reference

[1] G.A. Bell, J. Howell, T.W.D. Pesco, in: L.R. Rudnick, R.L. Shubkin (Eds.), Synthetic Lubricants and High-Performance Functional Fluids, Marcel Dekker Inc., New York, 1999, p. 215.
[2] Y. Tanaka, et al. Int. J. Thermophys. 10 (1989) 857.
[3] R.N. Kono, et al. IEEE Trans. Magnet. 37 (2001) 1827.
[4] W.R. Jones, et al. Ind. Eng. Chem. Res. 27 (1988) 1497.
[5] S.T. Cui, P.T. Cummings, H.D. Cochran, J. Chem. Phys. 104 (1996) 255.
[6] C. Baig, B.J. Edwards, D.J. Keffer, H.D. Cochran, J. Chem. Phys. 122 (2005) 184906.
[7] P.J. Daivis, D.J. Evans, J. Chem. Phys. 100 (1994) 541.
[8] H.-C. Li, et al. Mol. Phys. 100 (2002) 265.
[9] H.-C. Li, et al. Mol. Phys. 101 (2003) 2157.
[10] C. McCabe, et al. Ind. Eng. Chem. Res. 42 (2003) 6956.
[11] A. Koike, J. Phys. Chem. B 103 (1999) 4578.
[12] D. Kamei, et al. Tribol. Int. 36 (2003) 297.
[13] A.K. Rappe, et al. J. Am. Chem. Soc. 114 (1992) 10024.
[14] M. Tuckerman, B.J. Berne, G.J. Martyna, J. Chem. Phys. 97 (1992) 1990.
[15] D. Nosé, Mol. Phys. 52 (1984) 255.
[16] S. Nosé, J. Chem. Phys. 81 (1984) 511.
[17] W.G. Hoover, Phys. Rev. A 31 (1985) 1695.
[18] D.J. Evans, G.P. Morris, Statistical Mechanics of Nonequilibrium Liquids, Academic, New York, 1990.
[19] C. Baig, B.J. Edwards, D.J. Keffer, H.D. Cochran, J. Chem. Phys. 122 (2005) 114103.
[20] A.W. Lees, S.F. Edwards, J. Phys. Chem. B 5 (1972) 1921.
[21] Fomblin PFPE Lubricants Product Data Sheet, Solvay Solexis Co., 2004, http://www.solvaysolexis.com/pdf/fom_lube.pdf.
[22] J.L. Adcock, X.L. Cherry, J. Fluorine Chem. 30 (1985) 343.
[23] N. Crawford, J.L. Adcock, personal communication, 2005.
[24] J.M. Haile, Molecular Dynamics Simulation: Elementary Methods, John Wiley & Sons Inc., New York, 1992.
[25] D.I. Bower, An Introduction to Polymer Physics, Cambridge University Press, Cambridge, UK, 2002.
[26] A.N. Beris, B.J. Edwards, Thermodynamics of Flowing Systems with Internal Microstructure, Oxford University Press, New York, 1994.
[27] S.T. Cui, S.A. Gupta, P.T. Cummings, J. Chem. Phys. 105 (1996) 1214.